



Harnessing the thermogalvanic effect of the ferro/ferricyanide redox couple in a thermally chargeable supercapacitor

Arpan Kundu ^a, Timothy S. Fisher ^{b,*}

^a School of Mechanical Engineering, Purdue University, West Lafayette, IN 47907, USA

^b Mechanical and Aerospace Engineering Department, Los Angeles, CA 90095, USA

ARTICLE INFO

Article history:

Received 14 February 2018

Received in revised form

3 May 2018

Accepted 24 May 2018

Available online 30 May 2018

Keywords:

Thermogalvanic effect

Thermal charging

Supercapacitor

Redox electrolyte

Equivalent circuit

Fitting analysis

ABSTRACT

We report a high energy density thermally chargeable supercapacitor (TCSC) based on the thermogalvanic effect, built by sandwiching a potassium ferrocyanide/ferricyanide gel electrolyte film between two high surface area carbon cloth electrodes. In addition to the characteristic Seebeck coefficient of -1.21 mV K^{-1} , the pseudocapacitive property of the ferrocyanide/ferricyanide redox couple endows the device with a high area-specific capacitance of 13 F cm^{-2} which finally leads to high thermally induced energy storage density. Furthermore, the all-solid-state and flexibility of the device allows it to accommodate different heat source shapes. Overall, the device offers a simple, scalable and cost-effective means to harvest energy from intermittent waste heat sources. Lastly, we propose an equivalent circuit model to elucidate the working mechanisms of energy conversion and storage applicable to thermally chargeable supercapacitor devices in general. A fitting analysis aids in the evaluation of model circuit parameters providing good agreement with experimental voltage and current measurements.

© 2018 Published by Elsevier Ltd.

1. Introduction

The requirements of today's portable and wearable electronic equipment have prompted the need to integrate 'on-chip' energy storage devices [1,2]. Integrated power sources are required for autonomous or semi-autonomous microdevices used for remote sensing and implantable electrophysiology. One viable path to avoid the need for charging such power sources with external power supply is to harness energy from low-grade waste heat that is abundantly available from various sources such as solar energy or body heat. Conventional thermoelectrics, typically inorganic semiconductors, are expensive which exhibit low Seebeck coefficients ($10\text{--}100 \mu\text{V/K}$). Hence new routes for thermoelectric conversion are being explored such as thermally driven ion migration [3–6], mixed ion/electron diffusion [7,8] thermogalvanic [9,10] and thermomagnetic [11] effects.

Thermo-electrochemical cells (or thermocells) that exploit the thermogalvanic effect are quite attractive due to their low cost, simple design and operation near room temperature. Such devices based on the thermogalvanic effect generate steady electrical

power upon application of a temperature gradient across two electrodes. The thermogalvanic Seebeck coefficient S_e due to a generic electron transfer reaction $B \rightarrow A + ne^-$ is

$$S_e = \frac{\partial V}{\partial T} = \frac{\Delta S_{B,A}}{nF}, \quad (1)$$

where V is electrode potential, T is temperature, $\Delta S_{B,A}$ is the reaction entropy for the redox couple, n is the number of electrons involved in the reaction, and F is the Faraday constant. Ikeshoji [12], Quickenden [13] and Burrow [14] were the first to report a high S_e value of -1.4 mV K^{-1} for ferrocyanide/ferricyanide aqueous solutions; this value is approximately one order of magnitude higher than those reported for conventional thermoelectric materials such as Bi_2Te_3 (ca. 0.2 mV K^{-1} [15]). Significantly high Seebeck coefficients have also been reported for electrolytes composed of cobalt complexes [16] (1.9 mV K^{-1}) and triiodides [17] (2.0 mV K^{-1}).

In the past, researchers have demonstrated thermocells with enhanced performance by employing large surface area carbon electrodes [18–20]. The most widely used electrolyte was aqueous ferrocyanide/ferricyanide due to its favourable properties, namely high Seebeck coefficient, low cost and high ionic conductivity. Furthermore, in order to boost the overall conversion efficiency, the electrical and thermal resistances were tuned by introducing

* Corresponding author.

E-mail address: tsfisher@ucla.edu (T.S. Fisher).

conductive additives into the aqueous medium [9,21]. However, such aqueous electrolytes make large-scale integration and packaging cumbersome. Solid-state polymer gel electrolytes, in contrast, offer easy handling, improved safety, low internal corrosion, lightness, shape versatility and manufacturing simplicity. In a past report, Yang et al. [22] fabricated a pair of thermogalvanic gel electrolytes for use in wearable thermocells.

Although thermocells can generate continuous power from a steady temperature gradient, for intermittent sources additional energy storage devices are required to store the harvested energy. Recent studies have attempted to integrate both functionalities into a single device leading to overall system simplicity and suitability for waste heat harvesting. Zhao et al. [3,4] demonstrated thermal charging with PEO-NaOH liquid polymeric electrolyte operating on the basis of Soret effect with a Seebeck coefficient greater than 11 mV K^{-1} . Similarly, Kim et al. [23] fabricated a thermally chargeable solid-state supercapacitor with polystyrene sulfonic acid electrolyte exhibiting a Seebeck coefficient of 8 mV K^{-1} . However, Zhao's device suffered from high self-discharge rates and other drawbacks associated with liquid electrolytes. Kim's solid-state device, the first of its kind, consisted of polyaniline coated electrodes that are expensive and complicated to implement. Moreover, the high thermo-induced voltage demonstrated in these studies does not translate to high energy density. Although the converted voltage can be easily amplified using an inexpensive voltage converter circuit, the low amount of stored energy is unaltered by voltage conversion.

A TCSC's net energy density [24] expressed as $E = 1/2C(\Delta T)^2$ is influenced by both its capacitance C and Seebeck coefficient S . The conventional approach to obtain high capacitance involves constructing electrodes consisting of electrochemically active materials coated on carbon materials with high surface area (e.g., graphene [25], activated carbon [26], carbon nanotubes [27], carbon fibers [28], vertical graphene nanosheets or graphene petals (GPs) [29]). However, such electrodes can exhibit low electrical conductivity and poor cyclic stability [30]. An innovative approach involves introducing redox additives such as quinone/hydroquinone [31,32] or p-phenylenediamine [33,34] into liquid or gel electrolyte that enhance capacitance through electron transfer redox reactions. Interestingly, the ferro/ferricyanide redox couple, in addition to being used as an electrolyte in thermocells for its thermogalvanic effect, also finds application as a redox additive to electrolytes in supercapacitors [35–37]. The electron transfer reaction at the electrode/electrolyte interface $\text{Fe}(\text{CN})_6^{3-} + \text{e}^- \rightleftharpoons \text{Fe}(\text{CN})_6^{4-}$ is found to be highly reversible and produces a considerable improvement in the overall capacitance. Ma et al. [37] found that the addition of potassium ferricyanide to PVA/KOH gel electrolyte improved ionic conductivity and increased capacitance from 137.8 F g^{-1} to 431 F g^{-1} . To date, this redox couple has not been systematically employed in any device to exploit both its thermogalvanic and pseudocapacitive properties at the same time.

In the present work, we combine this new thermogalvanic gel electrolyte, PVA/ $\text{K}_3\text{Fe}(\text{CN})_6/\text{K}_4\text{Fe}(\text{CN})_6$, with inexpensive carbon cloth electrodes to build an all-solid-state, lightweight, flexible thermally chargeable supercapacitor (TCSC). This device can be used as a stand-alone component to store charge from intermittent temperature gradients and subsequently supply on-demand power to portable electronic devices. It possesses high overall area-specific capacitance and low self-discharge rate, resulting in high energy density that can be harvested with minimum loss over a long period of time after 'thermal' charging. An equivalent circuit model of the device is also presented that produces voltage and current profiles similar to experimental measurements.

2. Results and discussion

2.1. Electrochemical characterization of electrodes

Carbon cloth (CC) has previously been employed as electrodes for supercapacitors primarily due to its large surface area. Scanning electron microscopy (SEM) images in Fig. S1 reveal the microstructure of pure carbon cloth at low and high magnifications. The average diameter of a single carbon fiber inferred from Fig. S1c is $\approx 9 \mu\text{m}$. The porous nature of the carbon cloth allows for a large number of reaction sites for the ferro/ferricyanide ions to exchange electrons leading to large overall capacitance. In order to enhance the electrochemical surface area, vertical graphene nanosheets or graphitic petals (GPs) were grown on the bare carbon cloth substrate in a microwave plasma chemical vapor deposition (MPCVD) system. In the past [38], carbon cloth coated with graphene petals (CC/GP) has shown promising results in supercapacitor applications. SEM images in Fig. S2 show the microstructure of GPs fully covering carbon cloth, which illustrates that the GPs grow approximately 300 nm from the carbon fibers. The measured Brunauer-Emmett-Teller (BET) surface area of CC/GP ($0.33 \text{ m}^2 \text{ g}^{-1}$) is approximately 3 times that measured for bare CC ($0.11 \text{ m}^2 \text{ g}^{-1}$).

The influence of electrolyte on the overall electrochemical performance is investigated by performing cyclic voltammetry tests in a three-electrode configuration cell over a voltage window of 0–0.8 V, for two different electrolytes: (i) $0.2 \text{ mol l}^{-1} \text{ K}_3\text{Fe}(\text{CN})_6/\text{K}_4\text{Fe}(\text{CN})_6$ (PFC) and (ii) $1.0 \text{ mol l}^{-1} \text{ H}_3\text{PO}_4$. Furthermore, separate experiments were conducted for bare CC and CC/GP electrodes in order to evaluate the contribution of the GPs to charge storage. The results of CV tests performed at a scan rate of 50 mV s^{-1} with bare CC and CC/GP electrodes in PFC electrolyte are shown in Fig. 1a, while results of CV tests with H_3PO_4 electrolyte are shown in Fig. 1b. The CV curves for the PFC electrolyte exhibit sharp redox peaks at around 0.7 V which may be attributed to redox reaction through direct electron transfer process from $\text{Fe}(\text{CN})_6^{4-}$ to $\text{Fe}(\text{CN})_6^{3-}$. On the other hand, the CV curves for the H_3PO_4 electrolyte exhibit a more rectangular shape indicating only electrical double-layer contribution.

The area-normalized specific capacitance derived from the CV curves is shown as a function of scan rate in Fig. 1c and d for PFC electrolyte and H_3PO_4 electrolyte respectively. At a scan rate of 5 mV s^{-1} , the area-normalized capacitance obtained with bare carbon cloth electrode in PFC electrolyte is evaluated to be 2.8 F cm^{-2} . The specific capacitance based on the total mass of a single bare CC electrode is calculated to be 156.7 F g^{-1} . These values can be observed to be almost 10 times greater than that obtained with bare CC electrode in H_3PO_4 electrolyte. Such high capacitance can be attributed to the pseudocapacitive charge storage mechanism of the redox ions present in the PFC electrolyte. The capacitance value declines rapidly for the PFC electrolyte with rise in scan rate. At a scan rate of 100 mV s^{-1} , the areal capacitance value is 0.25 F cm^{-2} for PFC electrolyte which is merely 4 times that for H_3PO_4 electrolyte. Past studies [39,40] suggest that such capacitance decay may be attributed to incomplete participation of the ferrocyanide/ferricyanide ions in charge storage during rapid cycling.

Fig. 1c shows that the capacitance values computed for H_3PO_4 electrolyte are significantly larger in case of CC/GP electrode compared to bare CC electrode. The CC/GP electrode offers a capacitance improvement of 2.3 and 5.9 times at scan rates of 2 and 100 mV s^{-1} respectively, which is indicative of GPs offering larger electroactive surface area to ions present in the H_3PO_4 electrolyte. However, as shown in Fig. 1d, for PFC electrolyte, the GPs offer a minor improvement in capacitance at all scan rates. Such result for

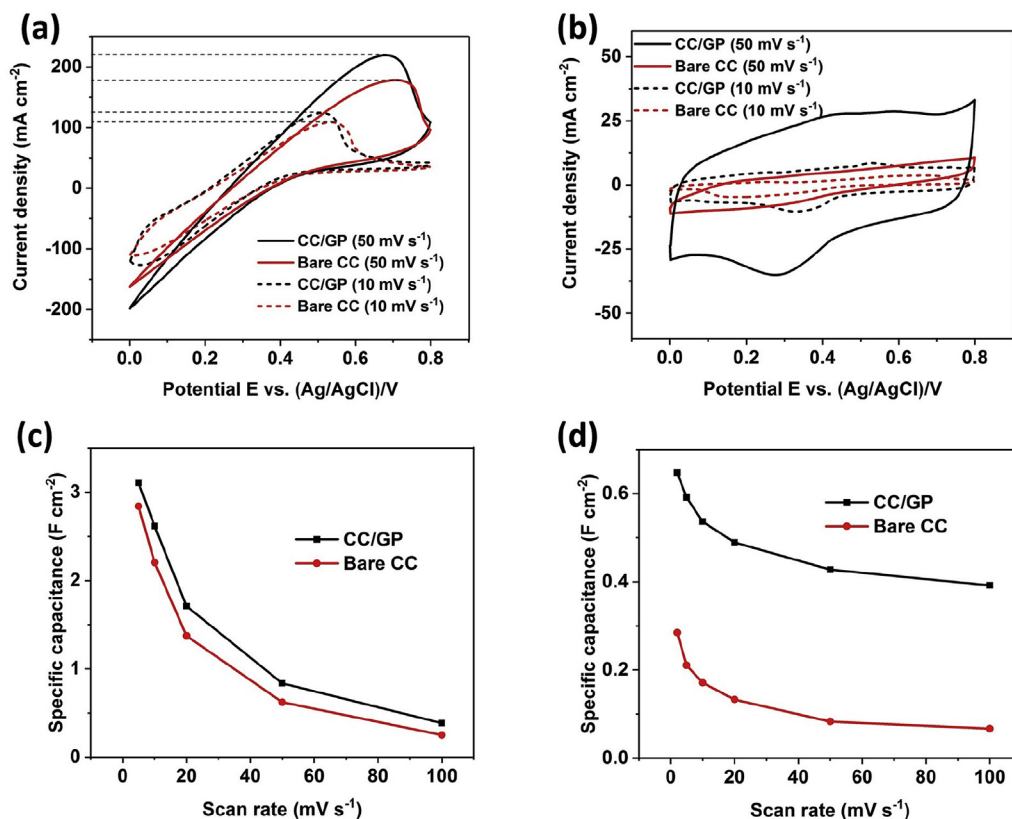


Fig. 1. Electrochemical performance of bare carbon cloth (CC) and graphene petal coated carbon cloth (CC/GP) electrodes in a three electrode configuration. (a) CV curves for bare CC and CC/GP electrode at scan rates of 10 mV s^{-1} and 50 mV s^{-1} in mixture of $0.2 \text{ mol l}^{-1} \text{ K}_3\text{Fe}(\text{CN})_6$ and $0.2 \text{ mol l}^{-1} \text{ K}_4\text{Fe}(\text{CN})_6$ (PFC) (b) CV curves for bare CC and CC/GP electrode at scan rates of 10 mV s^{-1} and 50 mV s^{-1} in $1.0 \text{ mol l}^{-1} \text{ H}_3\text{PO}_4$ aqueous solution (c) Comparison of area-normalized specific capacitance obtained with bare CC and CC/GP electrodes at different scan rates in aqueous PFC electrolyte (d) Comparison of area-normalized specific capacitance of bare CC and CC/GP electrodes at different scan rates in $1.0 \text{ mol l}^{-1} \text{ H}_3\text{PO}_4$ aqueous electrolyte.

ferrocyanide/ferricyanide electrolyte has been previously attributed to the fact that the redox reactions at the electrode/electrolyte interface are diffusion controlled and the diffusion layer thickness is generally much larger than the size of the nanostructures present at the electrode surface [41,42].

2.2. Thermally chargeable supercapacitor based on PVA/ $\text{K}_3\text{Fe}(\text{CN})_6/\text{K}_4\text{Fe}(\text{CN})_6$ polymer gel electrolyte

The all-solid-state symmetric supercapacitor device used to demonstrate thermal charging was fabricated by sandwiching a piece of gel electrolyte film between two bare carbon cloth electrodes. The typical dimensions of each electrode were $15 \text{ mm} \times 5 \text{ mm}$. The gel electrolyte was composed of an aqueous solution of poly(vinyl alcohol) (PVA) and potassium ferricyanide/ferrocyanide redox couple (see Experimental section for preparation details). It serves the dual purpose of a solid electrolyte and a thermoelectric generator. The device was encased in a nylon film package to prevent electrolyte evaporation. The assembly consisting of the electrodes, gel film, nylon film packaging, fabrics and copper wires is flexible and pliable enough to accommodate a wide variety of heat source shapes. A sketch depicting the structure of the flexible TCSC is provided in Fig. 4a.

Before testing the thermoelectric properties of the two-terminal symmetric device, its electrochemical performance was characterized using galvanostatic charge/discharge (GCD), cyclic voltammetry (CV), electrochemical impedance spectroscopy (EIS) and cyclic stability tests. Galvanostatic charge/discharge (GCD) profiles

are shown in Fig. 2a for current densities ranging from 0.2 to 1.0 mA cm^{-2} in the potential window of 0 and 0.1 V (profile at current density of 0.1 mA cm^{-2} shown in Fig. S3a). The semi-symmetric shape of the charge/discharge curves is indicative of high Coulombic efficiency and stable capacitance. The area-normalized specific capacitance can be derived from the curves using the relation [43],

$$C_{s1} = \frac{I_d}{\nu}, \quad (2)$$

where I_d is the discharge current density and ν is the slope of the voltage profile after the IR drop. C_{s1} is shown as a function of the charge/discharge rate (current density) in Fig. 2c.

At a constant current density of 0.1 mA cm^{-2} , the calculated area-specific capacitance is 9.5 F cm^{-2} . This value is more than an order of magnitude higher than what was obtained in the past two studies on thermally chargeable supercapacitors [3,23]. It can be attributed to the pseudocapacitive contribution of the redox species which are absent in case of pure double-layer electrolytes. Furthermore, the area-specific capacitance shows a decreasing trend with discharge current density because of the dominance of charge transfer polarization and concentration (mass transfer) polarization at high scan rates [40]. We note in this context that area-normalized specific capacitance rather than mass-based specific capacitance is generally more important to consider in wearable applications [44–46]. The internal resistance calculated based on the IR voltage drop at the beginning of discharge (shown in Fig. S3b) is 71Ω at a current density of 1 mA cm^{-2} which can be

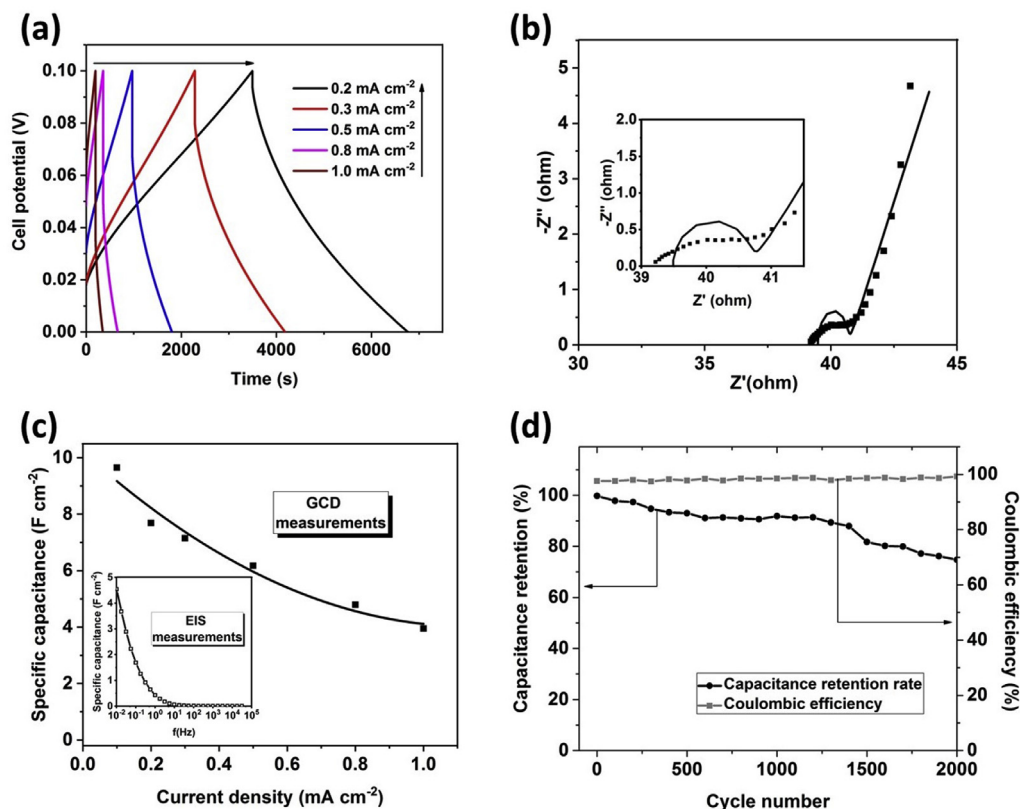


Fig. 2. Electrochemical performance of an all-solid-state two-terminal symmetric supercapacitor device composed of bare carbon cloth electrodes and 1.5 mm thick gel electrolyte film. (a) Galvanostatic charge-discharge (GCD) curves at constant-current densities ranging from 0.2 to 1.0 mA cm⁻². (b) Nyquist plot in the frequency range of 10 mHz and 100 kHz. (c) Area-specific capacitance versus current density obtained from the GCD curves. The inset shows area-specific capacitance vs frequency obtained from Nyquist plot. (d) Charge/discharge cycling test performed at a current density of 5 mA cm⁻² over the voltage range of 0–1.0 V, showing ≈ 8% loss over 1000 cycles and ≈ 25% loss after 2000 cycles.

considered quite large and is caused by the low ionic conductivity of the gel electrolyte.

Electrical impedance spectroscopy was carried out to probe the electrochemical behavior of the device in the frequency range of 10 mHz and 100 kHz with ac voltage amplitude set at 5 mV and dc bias at 0 mV. As shown in Fig. 2b, the Nyquist plot displays the variation of the imaginary part of impedance, $-Z''(f)$ vs. the real part of the impedance $Z'(f)$ where f is the frequency. The plot consists of two distinct segments: a distorted semicircle in the high frequency region and a sloped line in the low frequency region. The x -intercept in the plot represents the internal resistance of the electrode material and electrolyte of the device, while the semicircle represents the charge transfer resistance corresponding to the Faradaic reaction occurring at the electrode/electrolyte interface. The slope of the line in the low frequency region is around 53° which is much lower than 90° exhibited by a pure capacitor. Such deviation from a straight vertical line is indicative of diffusion-controlled reactions [10]. The area-specific capacitance derived from the Nyquist plot using the relation [47],

$$C_{s2} = -1/(2\pi fAZ'') \quad (3)$$

is shown as a function of frequency in the inset of Fig. 3c. Following the trend of C_{s1} , the calculated value decreases from 5.7 F cm⁻² at a frequency of 10 mHz to 1.5 F cm⁻² at a frequency of 1 Hz. Long-term cyclic life is a crucial factor for practical applicability of such devices. The cyclic stability tests for the device at a constant current density of 5 mA cm⁻² show a mere 8% loss in specific capacitance after 1000 cycles and 25% loss after 2000 charge-discharge cycles with ≈ 100% Coulombic efficiency as shown in Fig. 2d. The

capacitance decay can be attributed to the increasing aggregation of ferrocyanide/ferricyanide ions in the electrode pores, while the high coulombic efficiencies are representative of ultra-fast reaction kinetics at the electrode/electrolyte interface [37].

In Section 2.1, it was deduced from three-electrode measurements, that CC/GP electrode exhibits a marginal improvement in electrochemical performance over bare CC electrode in aqueous PFC electrolyte. A similar comparison study has been performed for the solid-state TCSC devices. Fig. 3a displays a comparison of galvanostatic charge/discharge (GCD) curves recorded for two devices: (i) a solid-state supercapacitor device composed of PVA/K₃Fe(CN)₆/K₄Fe(CN)₆ gel electrolyte and bare CC electrodes and (ii) a solid-state supercapacitor device composed of PVA/K₃Fe(CN)₆/K₄Fe(CN)₆ gel electrolyte and CC/GP electrodes. The two GCD profiles predominantly overlap one another, indicating that the CC/GP electrodes do not exhibit substantial improvement in electrochemical performance over bare CC electrodes. Such an observation can be attributed to the diffusion-controlled nature of the redox electrolyte [48,49]. The specific capacitances are computed to be 9.7 and 9.8 F cm⁻² respectively for the devices composed of bare CC and CC/GP electrodes. Fig. 3b contains cyclic voltammetry results obtained for the bare CC device at scan rates of 2 and 5 mV s⁻¹. The current peaks as a function of scan rate follow a scan rate^{0.57} power law relation, which is very close to the square-root relation expected for an ideal diffusion-controlled reaction. Therefore, these results suggest that the Fe(CN)₆³⁻/Fe(CN)₆⁴⁻ ions present in the PVA/K₃Fe(CN)₆/K₄Fe(CN)₆ gel electrolyte engage in a diffusion-controlled reaction at the electrode surface during charge/discharge. Because the GPs contribute marginally to the performance, bare CC is used to prepare electrodes for the TCSC device.

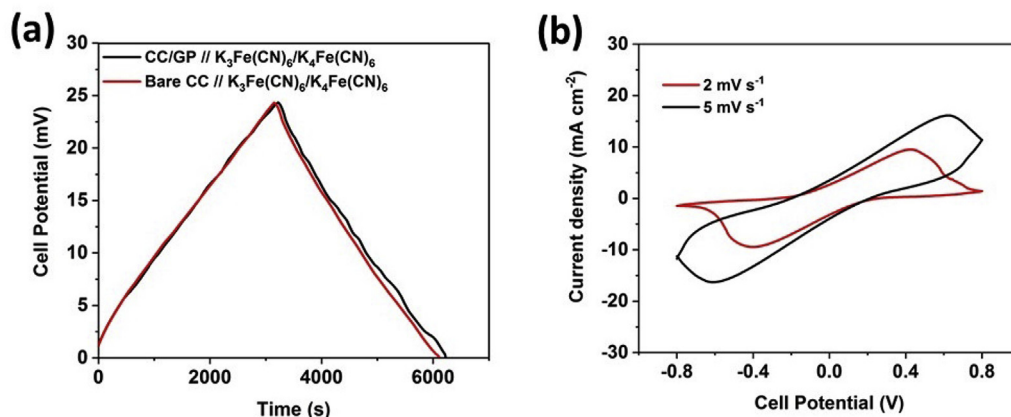


Fig. 3. (a) Comparison of GCD profiles obtained at an operating current density of 0.1 mA cm^{-2} over the voltage window of 0–25 mV recorded for the symmetric two-terminal TCSC devices composed of bare CC electrodes and CC/GP electrodes. A 1.5 mm thick film of PVA/K₃Fe(CN)₆/K₄Fe(CN)₆ gel electrolyte is used to fabricate both the TCSC devices. (b) Cyclic voltammetry curves measured for TCSC device composed of bare CC electrodes performed at scan rates of 2 and 5 mV s^{-1} over a voltage range of –0.8 V to +0.8 V.

The thermoelectric properties of the device are tested by sandwiching it in between a Peltier heater and cooler as shown in Fig. 4b. A thermistor is attached to each face of the external casing in order to monitor the applied temperature difference ΔT_{ext} . The open circuit thermovoltage V_{oc} is recorded for different values of applied ΔT_{ext} by varying the hot and cold side temperatures. The absolute values of the hot and cold side temperatures are listed in Table S1. The transient plot shown in Fig. 4c reveals that the open circuit voltage V_{oc} closely follows the variation of the applied temperature gradient ΔT_{ext} with respect to time. Furthermore, the steady state value of thermo-induced voltage was recorded for

different ΔT_{ext} values (each held fixed for 3 min). The plot shown in Fig. 4d establishes a linear relationship between the steady-state V_{oc} and the applied temperature difference ΔT_{ext} in both positive and negative regimes. The effective Seebeck coefficient S_{eff} , is then back-calculated using the measured open circuit voltage V_{oc} and the applied temperature difference ΔT_{ext} through

$$S_{\text{eff}} = \frac{V_{\text{oc}}}{\Delta T_{\text{ext}}} \quad (4)$$

As expected, the S_{eff} magnitude evaluated from the slope,

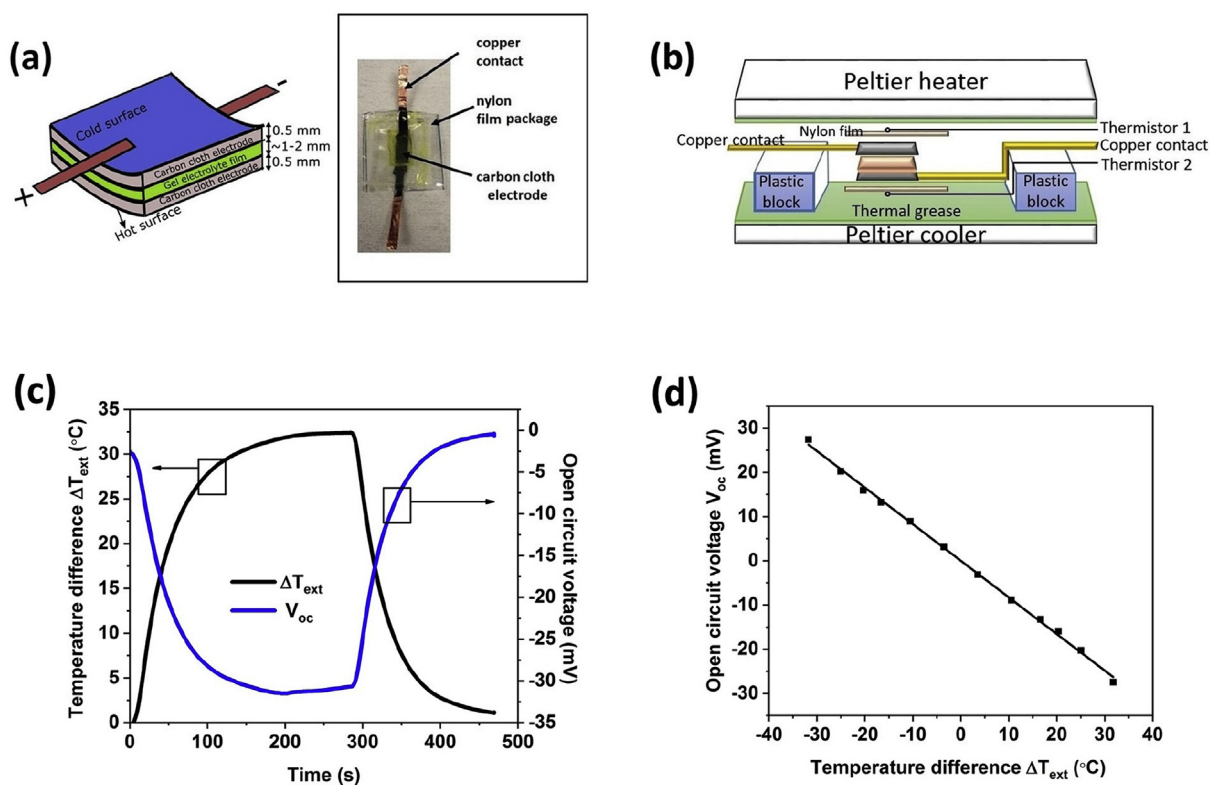


Fig. 4. (a) Sketch of the thermally chargeable supercapacitor (TCSC) and photograph of the actual device in inset. (b) Schematic of the test platform used for thermoelectric measurements. (c) and (d) show thermoelectric properties of the TCSC device composed of bare carbon cloth electrodes and 1.5 mm thick PFC gel electrolyte film. Plot of recorded open-circuit voltage V_{oc} and applied temperature difference ΔT_{ext} as a function of time is displayed in (c), while the plot of steady state V_{oc} versus ΔT_{ext} is shown in (d).

0.86 mV K⁻¹ is lower than the characteristic Seebeck coefficient of the ferrocyanide/ferricyanide redox couple (1.21 mV K⁻¹). The ratio between the two is 0.71 which is about a factor of 7 higher than found for a plastic thermocell based on ferrocyanide/ferricyanide redox electrolyte [10].

2.3. Thermally chargeable supercapacitor design parameters

Cyclic voltammetry tests performed in a three-electrode configuration cell described previously in Section 2.1 illustrate the role of the ferrocyanide/ferricyanide ions present in the aqueous electrolyte in providing additional pseudocapacitance. In addition to double-layer formation, the ions engage in redox reactions at the electrode/electrolyte interface during charge/discharge that results in enhanced capacitance. In order to confirm the pseudocapacitive behavior of the ferrocyanide/ferricyanide redox couple present in the gel electrolyte, a comparison of electrochemical performance is conducted between solid-state devices composed of PVA/H₃PO₄ and PVA/K₃Fe(CN)₆/K₄Fe(CN)₆ gel electrolyte films each 1.5 mm thick. Both devices are built of bare CC electrodes. The galvanostatic charge/discharge (GCD) curves corresponding to a current density of 1 mA cm⁻² are displayed in Fig. S4. For both devices, the curves are symmetric in nature. However, the curve for the redox electrolyte exhibits a larger area that corresponds to larger capacitance. The areal capacitance value is evaluated to be 5.5 F cm⁻² for the device composed of PVA/K₃Fe(CN)₆/K₄Fe(CN)₆ gel electrolyte and 0.167 F cm⁻² for the device composed of PVA/H₃PO₄ gel electrolyte. Thus, the pseudocapacitive contribution of the ferrocyanide/ferricyanide ions leads to 33 times higher capacitance for a small operating current density of 1 mA cm⁻².

The thickness of the gel electrolyte film plays a major role in determining the device performance. A thick film is expected to lead to a large value of temperature difference ΔT_{act} induced across

the two faces of the gel electrolyte film in response to the same applied ΔT_{ext} applied across the device, which is expected to lead to a high value of effective Seebeck coefficient S_{eff} . However, a large thickness is expected to adversely affect ion transport in the electrolyte leading to poor areal capacitance. As explained earlier, the energy storage in the device is proportional to the product of areal capacitance and square of S_{eff} . Therefore, both parameters need to be maximized in order to attain high energy storage density. Here, we have investigated these two performance parameters separately for devices with film thickness values of 0.3 mm, 0.9 mm and 1.5 mm. Fig. 5a shows the thermo-induced open circuit voltage V_{oc} as a function of ΔT_{ext} for the three devices. The thermo-induced V_{oc} can be observed to rise linearly with applied temperature gradient in all cases (time-dependent results shown in Fig. S6). However, the slope is much larger for the 0.9 mm film device compared to the 0.3 mm film device that corresponds to higher temperature difference induced across the two faces of the film. The slope increases marginally with rise in film thickness from 0.9 mm to 1.5 mm, which indicates that the ratio of the thermal resistance of the film to thermal resistance of the overall device does not vary significantly for film thickness greater than 0.9 mm.

Fig. 5b shows the galvanostatic charge/discharge curves for the three devices, all at a constant current density of 1 mA cm⁻². The areal capacitance derived from the CV curves is shown as a function of the gel film thickness in Fig. 5d. It can be observed that the areal capacitance drops in value with rise in film thickness. It decreases from a value of 8.6 F cm⁻² for a film thickness of 0.3 mm to a value of 5.5 F cm⁻² for a film thickness of 0.9 mm. In order to compare the thermally-induced energy storage for the films, the energy coefficient defined as $k = 1/2CS_{eff}^2$ is evaluated for all three devices. Fig. 5d shows that k follows the trend of the effective Seebeck coefficient and is highest for the 1.5 mm thick film. Therefore, we decided to use the 1.5 mm thick film in our thermoelectric

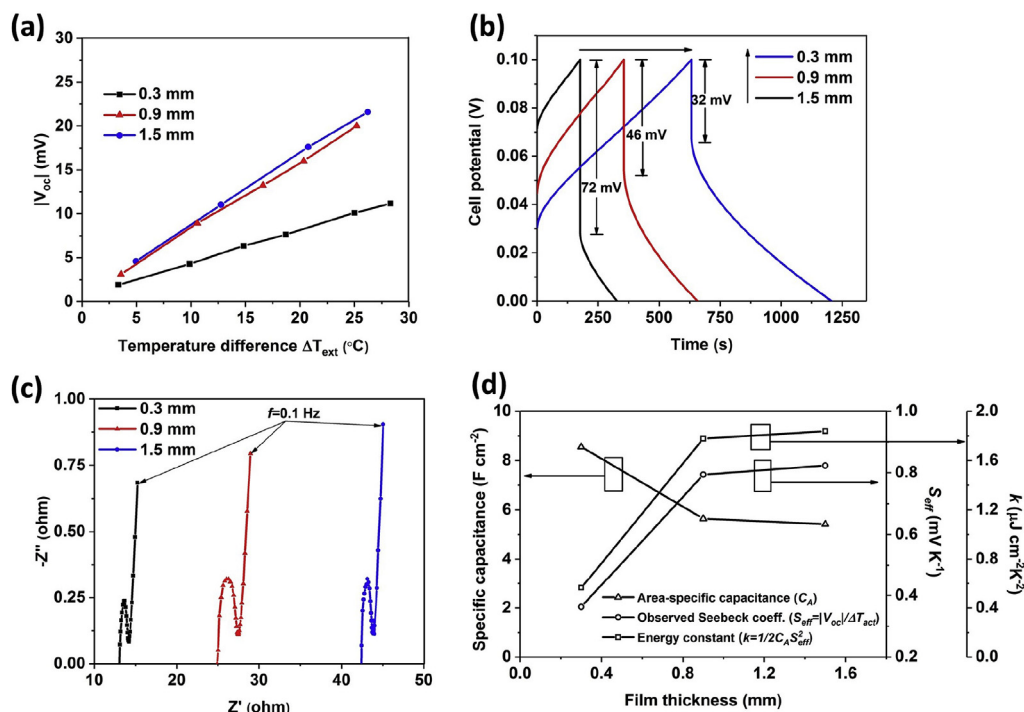


Fig. 5. (a) Thermally induced open circuit voltage as a function of the externally applied temperature gradient ΔT_{ext} for devices with gel film thickness 0.3 mm, 0.9 mm and 1.5 mm. (b) Galvanostatic charge/discharge profiles at a constant current density of 1 mA cm⁻² for devices with gel film thickness 0.3 mm, 0.9 mm and 1.5 mm. (c) Nyquist plots for EIS tests conducted in the frequency range of 0.1 Hz and 100 kHz for TCSC devices with film thickness 0.3 mm, 0.9 mm and 1.5 mm. (d) Areal capacitance, C_A derived from galvanostatic charge/discharge cycling at a current density of 1 mA cm⁻², effective Seebeck coefficient S_{eff} and energy constant $k = 1/2C_A S_{eff}^2$ plotted as a function of gel film thickness.

measurements.

The Nyquist plot shown in Fig. 5c exhibits rising value of x intercept with increase in film thickness. Using the slope of rise of the x intercept with thickness (shown in Fig. S7), the bulk ionic conductivity of the electrolyte using

$$\sigma = \frac{1}{s.A} \quad (5)$$

is estimated to be 5.44 mS cm^{-1} which is similar to the value determined by Yang et al. [22] for the same gel electrolyte (6 mS cm^{-1}) at room temperature. Here, s represents the slope of variation of x -intercept in the Nyquist plot with film thickness, and A is the projected area of each electrode.

2.4. Demonstration of thermal charging phenomenon

Fig. 6a shows the bias circuit used to investigate the thermal charging phenomenon. The device is connected in series with a variable resistor R_M while a temperature gradient ΔT_{ext} is applied across its two surfaces. The time variant voltage and current across the variable resistor is recorded with the help of data acquisition boards NI-DAQ 9215 and NI-DAQ 9203 respectively at a sampling rate of 100 samples per second.

Fig. 7 shows the measured transient electrical response of the device during one typical thermal charging cycle. In order to charge the device thermally, a steady temperature difference ΔT_{ext} of 50°C was applied across its faces, while shorting its two terminals

externally. The charging current density induced by the thermo-voltage jumps from 0 to -0.6 mA cm^{-2} in response to the applied temperature difference. As the device continues to charge gradually under application of the constant temperature difference, the current decays slowly to finally reach a value close to 0. The long charging time (3600 s) can be attributed to the high RC time constant of the device. The RC time constant can be minimized either by lowering the device resistance or the device capacitance. Because, high capacitance is mandatory for attaining high energy density, the only feasible way to decreasing the RC time constant is by lowering the device internal resistance which requires an improvement in the electrolyte ionic conductivity.

At the end of the thermal charging process, the circuit is opened and the voltage across the terminals is recorded as a function of time. As soon as the temperature gradient is removed, the open circuit voltage increases from 0 to 41 mV. Because of self-discharge, the thermo-induced open circuit voltage decays to 31 mV in the next 4100 s. We note that the observed charge retention capability compare favorably to a similar TCSC device [3] (decay from 150 mV to 0 in 1600s). Self-discharge in supercapacitors composed of potassium ferrocyanide/ferricyanide electrolyte has previously been attributed to the ability of the redox-active species to travel freely between the electrodes at open-circuit conditions [50].

Fig. 8 compares the thermo-induced voltage in two different runs with applied ΔT_{ext} values of 30 and 50°C . In both cases, the rise in thermo-induced voltage coincides with decline in the applied temperature difference. The thermo-induced V_{oc} for ΔT_{ext}

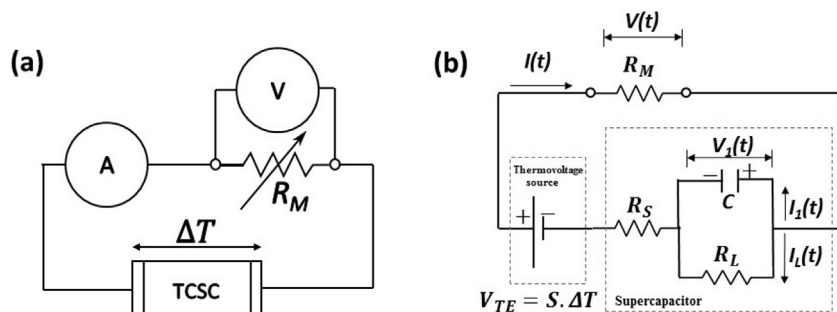


Fig. 6. (a) Bias circuit used for the thermoelectric measurements. (b) Equivalent circuit for the device and the load resistor. The device is modeled as a series combination of a thermo-induced voltage source and supercapacitor (represented by a Randles circuit).

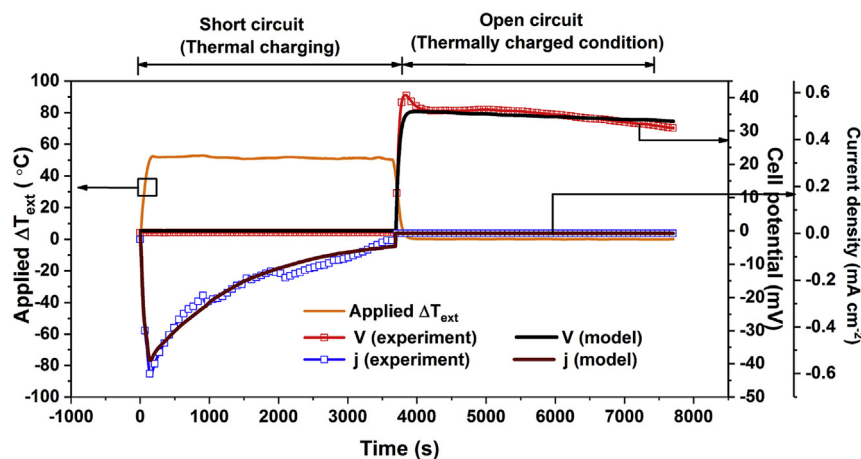


Fig. 7. Demonstration of thermal charging with a ΔT_{ext} value of 50°C . The thermistor reading on the cold and hot sides of the device during the thermal charging phase were 13°C and 63°C respectively. To begin with, the device is externally short-circuited while the temperature gradient is applied. When the charging current approaches zero, the circuit is opened and the temperature gradient is removed. The thermally charged V_{oc} is observed for a period of 5000s.

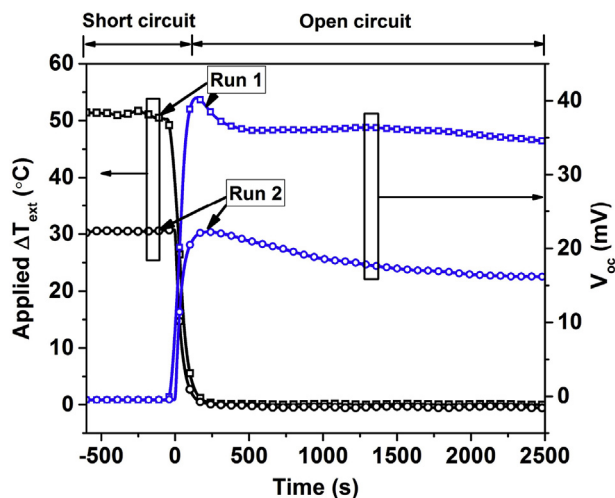


Fig. 8. Open circuit voltage profiles for two runs with ΔT_{ext} values of 50 °C and 30 °C. In both the runs, the device is thermally charged at a constant ΔT_{ext} under a short-circuit condition, following which the temperature gradient is removed and the open circuit voltage is measured.

30 °C peaks at 22.2 mV which slowly declines to 16.3 mV at the end of 2500 s due to self-discharge. Similarly, for $\Delta T_{ext} = 50$ °C, the thermo-induced V_{oc} starts from 40.4 mV and decays to 35 mV at the end of 2500 s. The decay in V_{oc} is comparatively less abrupt at the beginning for $\Delta T_{ext} = 30$ °C.

The working mechanism of the TCSC has been schematically described in Fig. 9. Initially, the gel electrolyte consists of ferrocyanide and ferricyanide ions randomly oriented in a polymer matrix (State 1). When the temperature of one electrode is raised with the aid of waste heat, it causes a change in the redox potential of the electrolyte, triggering the reaction $\text{Fe}(\text{CN})_6^{4-} \rightarrow \text{Fe}(\text{CN})_6^{3-} + e^-$. The reverse reaction does not occur at the cold electrode due to dearth of excess electrons. The accumulation of electrons at the hot electrode leads to a negative open circuit voltage (State 2). When the

electrodes are externally connected through a load resistor, electrons flow from the hot to cold electrode where they reduce the neighboring ferricyanide ions to ferrocyanide ions (State 3) while also generating some useful electrical work in the load resistor. This process represents ‘thermal charging’ of the supercapacitor and continues until the ion concentrations near the electrodes reach saturation, at which point the current through the external circuit decays to zero (State 4).

The reaction products remain localized near the hot and the cold electrodes due to their inability to travel through the tortuous path of the PVA polymer matrix. Such a characteristic is evidenced by the low ionic conductivity of the PVA/ $\text{K}_3\text{Fe}(\text{CN})_6/\text{K}_4\text{Fe}(\text{CN})_6$ gel electrolyte used in this work (6 mS cm^{-1} [22]) compared to that of $0.4 \text{ mol l}^{-1} \text{ K}_3\text{Fe}(\text{CN})_6/\text{K}_4\text{Fe}(\text{CN})_6$ aqueous electrolyte (170 mS cm^{-1} [9]). Upon removing the temperature gradient, both electrodes return to ambient temperature causing the electrolyte redox potential near the electrodes to change, this time in the direction opposite to State 2. The ferrocyanide ions near the cold electrode become oxidized to generate ferricyanide ions and electrons at the electrode, leading to a positive open circuit potential (State 5). We note that the reverse reaction does not occur at the hot electrode upon equilibration due to lack of excess electrons. State 5 represents the ‘thermally charged’ state of the supercapacitor.

2.5. Equivalent circuit model

The mechanism of TCSC operation explained in the previous subsection is further elucidated here with the help of an equivalent circuit model. Because the TCSC performs the dual function of a thermoelectric generator and a supercapacitor, we propose that it can be effectively modeled by a series combination of a thermo-induced voltage source and a supercapacitor. The supercapacitor is modeled as a Randles equivalent circuit as shown in Fig. 6b. The voltage source V_{TE} is assumed to be the product of the Seebeck coefficient S of the gel electrolyte and the temperature difference across the faces of the gel film, ΔT_{act} across the two surfaces of the gel electrolyte. S was found to be -1.21 mV K^{-1} for the gel electrolyte [22] over the range of ΔT from 0–20 K, and the same value is

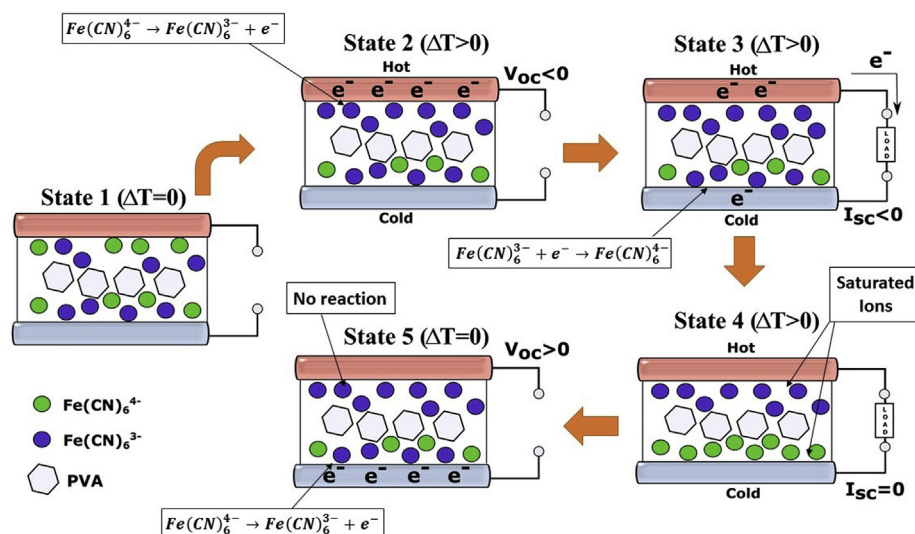


Fig. 9. Working mechanism of the thermally chargeable supercapacitor (TCSC). State 1: Discharged (initial) state with ferro/ferricyanide ions dispersed randomly in PVA matrix. State 2: When a temperature gradient is applied under open-circuit condition, the ferrocyanide ions at the hot electrode react to generate ferricyanide ions and electrons. State 3: Electrons generated by the reaction transfer to the cold side and reduce the neighboring ferricyanide ions to ferrocyanide ions upon shorting the two electrodes externally with a load resistor. State 4: The current drops to zero when all the ions on the hot (cold) side are oxidized (reduced). State 5: When the temperature gradient is removed and the load resistor is disengaged, the ferrocyanide ions at the cold electrode react to generate electrons. These electrons on the cold side produce an open circuit voltage present across the device at zero temperature gradient.

used here. The parameter R_S represents the ion transport resistance in the electrolyte, C represents an ideal capacitor at the electrode-electrolyte interface that stores charge during charging and releases charge during discharging, while R_L represents the leakage resistance in the device that causes self-discharge under an open-circuit condition. The load resistance used in the thermal charging and discharging phases are termed R_{mc} and R_{md} respectively. The voltage across the load resistor and the capacitor C are denoted by V and V_1 respectively. The current flowing through the load resistor, capacitor C and the leakage resistor R_L are represented by I , I_1 and I_L respectively. The model values of V and I across the load resistor are later used to validate the experimental results.

The timeline can be broken into 3 phases: thermal charging (Phase 1), hold (Phase 2) and discharge (Phase 3). Initially, the TCSC circuit is open, and both V_{TE} and V_1 are zero. In Phase 1, a load resistance R_{mc} is installed while maintaining a positive temperature gradient ΔT across the device. The thermo-induced voltage V_{TE} rises to ΔT , which then charges the capacitor C . The capacitor voltage V_1 increases gradually with time, while the charging current I decays slowly. The charging current is determined from

$$V_{TE} - V - V_1 - IR_S = 0. \quad (6)$$

In Phase 2, the temperature gradient is removed, and the external load is disengaged. This causes the thermovoltage V_{TE} to disappear and the open circuit voltage to attain the value of $-V_1$. Under open-circuit conditions, the TCSC should ideally maintain a constant voltage; however the presence of parasitic shunt paths in the device results in self-discharge that causes a slight decay in the open circuit voltage. V_1 is obtained from

$$\begin{aligned} I_L R_L + V_1 &= 0, \\ I_L &= C \frac{dV_1}{dt}. \end{aligned} \quad (7)$$

In Phase 3, the circuit is closed once again with a load resistor R_{md} , and the unknown voltage and current values are determined using

$$V_1 = -I(R_S + R_{md}). \quad (8)$$

Detailed analytical expressions of voltage and current across the load resistor during different phases of the cycle are listed in Eqs. (S1)–(S3). t'_1 , t'_2 and t'_3 represent time values from the beginning of Phases 1–3 respectively. The durations of Phases 1–3 are t_1 , t_2 , and t_3 respectively. The unknown parameters in the model are obtained by fitting expressions for voltage and current with the measurements. The procedure used for fitting is illustrated in Fig. 10. The

combination of parameters resulting in the minimum value of the total mean square error (MSE_{tot}) is selected to represent the circuit parameters. MSE_{tot} is chosen to be the sum of the normalized mean square error for voltage and for current, thereby giving them equal weight. The normalized MSE for the i th combination of parameters is defined as

$$MSE_{X,i} = \frac{\sum_{t=0}^{t=t_f} (X_{model,i}(t) - X_{exp}(t))^2}{\sum_{i=1}^n \sum_{t=0}^{t=t_f} (X_{model,i}(t) - X_{exp}(t))^2}, \quad (9)$$

where X stands for voltage or current, and n is the number of combinations of the fitting parameters.

Because the equivalent circuit is found to provide an excellent fit with the experimental results, it can be used as a convenient tool to analyze the role of the tunable parameters namely load resistance in the thermal charging phase R_{mc} , thermal charging phase duration, and hold phase duration. The performance indices obtained from the model are as follows.

The amount of charge stored in the capacitor in the thermal charging phase Q_c is obtained by integrating the capacitor charging current I_1 over time from 0 to t_1 . During charging, I_1 decreases exponentially with time while V_1 gradually rises to the equilibrium voltage. The value of Q_c upon complete charging ($I_1=0$) can be expressed as CV_{eff} where $V_{eff} = \Delta T \frac{R_L}{R_L + R_S}$. However, we note that the duration required for the device to charge completely may be quite long. For small charging durations, the capacitor is not completely charged by the end of the thermal charging phase. The charge released by the capacitor during discharge Q_{dc} is calculated by integrating I_1 with time from $(t_1 + t_2)$ to $(t_1 + t_2 + t_3)$. The charge retention ratio is defined as $\beta = \frac{Q_{dc}}{Q_c}$ and denotes the fraction of charge retained by the device during the hold phase.

The amount of energy supplied by the thermovoltage source during the thermal charging phase is given by

$$E_{in,ch} = \int_0^{t_1} I V_{TE} dt. \quad (10)$$

This energy is distributed among the circuit elements R_{mc} , R_S , C and R_L :

$$E_{in,ch} = E_{Rm,ch} + E_{C,ch} + E_{Rs,ch} + E_{Rl,ch} \quad (11)$$

$E_{Rs,ch}$ and $E_{Rl,ch}$ are energy losses in the series and leakage resistors, while $E_{Rm,ch}$ is the energy output in the load resistor. $E_{C,ch}$ is the energy stored in the capacitor. A fraction of this energy is lost during the hold phase due to current flow through the leakage resistance R_L . In the discharging phase, the stored energy is distributed among the load resistor R_{md} , series resistor R_S and the leakage resistor R_L . The thermovoltage source is absent in both the hold and discharging phases. The energy balance in the discharging phase can be written as,

$$-E_{C,dc} = E_{Rm,dc} + E_{Rs,dc} + E_{Rl,dc} \quad (12)$$

where $E_{C,dc}$ represents energy stored in the capacitor C , and $E_{Rm,dc}$, $E_{Rs,dc}$ and $E_{Rl,dc}$ represent energy lost in R_{md} , R_S and R_L respectively. A point to note here is that $E_{C,dc}$ is negative because the capacitor loses energy during discharge.

2.6. Model fitting

To estimate the areal capacitance of the TCSC device, model

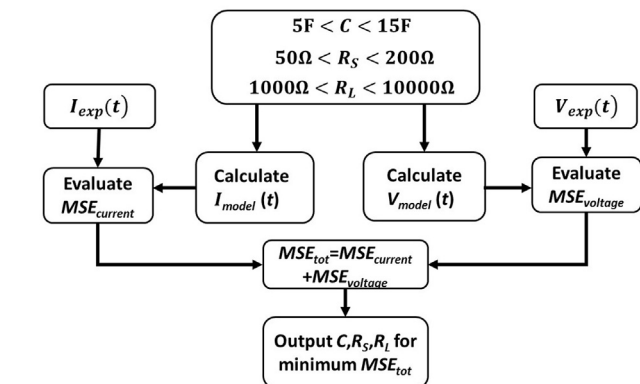


Fig. 10. Flow chart for calculating Randles circuit parameters for the thermally chargeable supercapacitor.

fitting based on the full equivalent circuit in Fig. 6b was performed on the measured voltage and current profiles. Current and voltage profiles were fitted by iterating over combinations of the free parameters in the Randles equivalent circuit. Values of the parameters that resulted in optimal voltage and current fit are: $R_S = 144 \Omega$, $R_L = 4100 \Omega$, $C = 10 \text{ F}$. Fig. 7 shows that the fitted model current and voltage profiles follow the experimental results quite closely. The value of MSE_{tot} obtained for the optimal fit is evaluated to be 6.59×10^{-5} , which is indicative of a very good fit. The areal capacitance 13.3 F cm^{-2} is comparable to that derived from galvanostatic charge/discharge cycling at a current density of 0.1 mA cm^{-2} (9.5 F cm^{-2}).

2.7. Stored charge and energy calculations

In Section 2.4, the thermal charging phenomenon was demonstrated by allowing the device to ‘thermally’ charge under closed circuit condition. Furthermore, the thermally induced open-circuit voltage was retained for a long time to investigate its self-discharge rate. This time, in order to estimate the amount of charge and energy stored in the TCSC device corresponding to the thermo-induced voltage, the ‘thermally’ charged TCSC device is connected in series to a load resistor after a hold period of 1000 s, and the voltage and current across the load resistor is monitored. Similar changes are made during the ‘thermal’ charging phase, the device is connected to a 330Ω resistor instead of short-circuiting. Thus, even during the ‘thermal’ charging stage, some useful amount of work is obtained. In principle, the load resistor can be varied to tune the useful work output and the charging speed of the device.

Fig. 11a displays the voltage profiles obtained across the load resistor corresponding to applied ΔT_{ext} values of 25, 35 and 50°C . The current profiles in phases 1 and 3 can be obtained by dividing the measured voltage V by R_M . The voltage variation is similar in all three runs and has a negative peak during phase 1 which thereafter slowly saturates to zero. Upon open-circuiting, the voltage rises to a positive value swiftly. This positive voltage value representing the thermo-induced voltage is discharged with a load resistor during the discharge phase. The output energies in phase 1, $E_{Rm,ch}$ and in phase 3, $E_{Rm,dc}$ are evaluated by integrating V^2/R_M with time. The negative peak voltage value as well as the charging time can be observed to rise with applied ΔT_{ext} . Similarly, the open circuit voltage during phase 2 increases proportionately with ΔT_{ext} . We

note that during the 1000 s hold time in phase 2, the decay is quite significant ($41.4\text{--}38.3 \text{ mV}$) for $\Delta T_{ext} = 50^\circ\text{C}$, while in the other two runs, the variation is marginal. The high self-discharge rate at high operating temperatures may be attributed to decrease in electrolyte viscosity and increase in thermal energy of ions at high temperatures [51]. During phase 3, the net discharge time (time until voltage dips below 1 mV) is higher for large values of ΔT_{ext} due to greater stored energy in the device.

The equivalent circuit model used to fit the measured voltage and current profiles may be perceived as a convenient tool to analyze the influence of controllable parameters such as the temperature difference across the faces of the gel film, ΔT_{act} , external load resistance during thermal charging R_{mc} , and hold phase duration. Fig. 11b shows the impact of the actual temperature difference ΔT_{act} across the electrolyte film on the charge and energy storage in the device during phase 1 and 3. The stored charge density in the capacitor element C rises approximately linearly with ΔT_{act} with a slope of $83 \text{ C m}^{-2}\text{K}^{-1}$. Owing to self-discharge during the hold phase, the output charge density in the discharge phase is lower with a slope of $58 \text{ C m}^{-2}\text{K}^{-1}$. The output charge in phase 3, evaluated from measurements shown in Fig. 11a can be observed to follow the trend of the model data.

The influence of the applied temperature gradient on the energy stored and energy output has also been evaluated using the model. Fig. 11b shows the variation of the energy output in the load resistor during thermal charging ($E_{Rm,ch}$), energy stored in the capacitor C during thermal charging ($E_{C,ch}$) and energy output in the discharge phase ($E_{Rm,dc}$). As expected, all three vary quadratically with the applied ΔT_{act} . Due to loss in the various circuit elements, $E_{Rm,dc}$ is lower than the stored energy $E_{C,ch}$. Furthermore, $E_{Rm,dc}$ calculated from the measured voltage profiles displayed in Fig. 11a, which is also shown in the same plot, shows a close resemblance to that calculated using the model.

A load resistance R_{mc} applied during the charging phase may be beneficial for extracting some useful work, although it may lead to low charging currents (Fig. S8b), implying slow charging rates. Consequently, with a rise in the value of the load resistance R_{mc} and considering a fixed thermal charging phase duration, the charge stored (Q_C) and energy stored ($E_{C,ch}$) decline due to insufficient charging, while the energy output during the thermal charging phase ($E_{Rm,ch}$) rises.

Fig. S9 displays the influence of the applied hold time on the

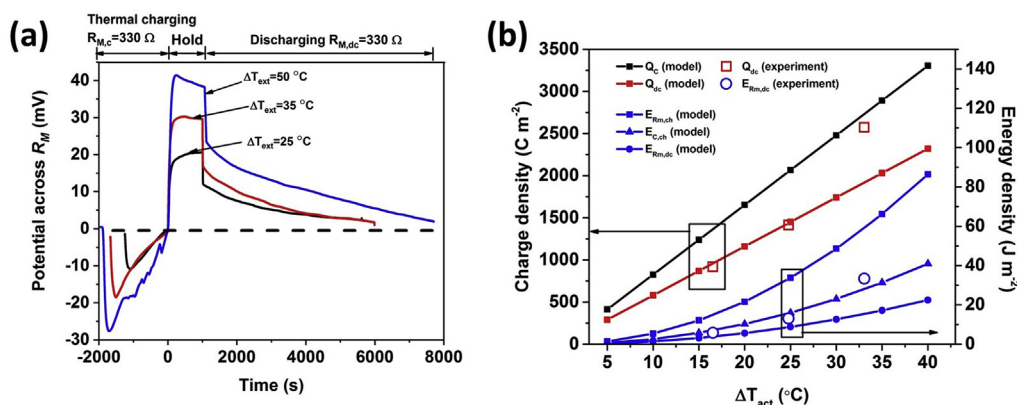


Fig. 11. (a) Measured voltage across the load resistor R_M corresponding to runs with ΔT_{ext} of 25, 35 and 50°C . Each run consists of a thermal charging phase, a hold phase and a discharging phase. The load resistance is set at 330Ω in both the thermal charging phase and the discharging phase. The hold phase duration is 1000 s. (b) Measured and modeled values of charge and energy storage density as a function of the temperature difference across the faces of the gel film, ΔT_{act} . The geometric area of the electrodes is used for normalization. Q_C denotes the charge input to the capacitor C in the thermal charging phase while Q_{dc} denotes the charge released by the capacitor in the discharging phase. $E_{C,ch}$ represents the energy stored in the capacitor C in the thermal charging phase, while $E_{Rm,ch}$ and $E_{Rm,dc}$ represent the energy output in the load resistance during thermal charging and discharging respectively.

Table 1Comparison of devices with different solid-state electrolytes for energy capture from intermittent heat sources for a ΔT_{act} of 10 °C.

Electrolyte	Capacitance C (F cm ⁻²)	Seebeck Coefficient S_e (mV K ⁻¹)	Energy stored $E_{ch} = \frac{1}{2} C(S_e \Delta T)^2$ (μJ cm ⁻²)	Charge stored $Q_{ch} = C(S_e \Delta T)$ (mC cm ⁻²)	Ref.
PEO-NaOH	0.00103	11.1	6.3	0.11	[3]
PSSH	0.12	7.2	311.0	8.64	[22]
PVA/K ₃ Fe(CN) ₆ /K ₄ Fe(CN) ₆	13.3	1.2	973.6	160.90	This Work

charge and energy output characteristics of the device. During the hold phase, the capacitor loses charge due to self-discharge through the leakage resistance R_L . This is due to decay in the capacitor voltage V_1 . The charge retention ratio and the energy retention ratio are given by $\beta_Q = Q_{dc}/Q_C$ and $\beta_E = E_{Rm,dc}/E_{C,ch}$ respectively. For zero hold time, β_Q is close to 100% while β_E is 62% because of energy loss in the circuit elements other than the load resistor, which occur even at zero hold time. With a rise in hold time from 0 to 3000s, the value of β_Q falls to 89%, while β_E falls to 54%.

2.8. Performance comparison

We now compare the performance parameters of our device with similar TCSC devices demonstrated in recent studies. Table 1 shows that the area-specific capacitance of our device (13.3 F cm⁻²) exceeds the PSSH device (120 mF cm⁻²) and the PEO-NaOH device (1031 μF cm⁻²) by 110 and 13000 times respectively. On the other hand, the Seebeck coefficient of our device (1.21 mV K⁻¹) is inferior to that for the PSSH device [23] (7.2 mV K⁻¹) and the PEO-NaOH device [3] (11.1 mV K⁻¹) by 6 and 10 times respectively. However, considering the effects of both areal capacitance and Seebeck coefficient, the net thermally induced charge and energy density values turn out to be much greater for our device compared to the PSSH device and the PEO-NaOH device. Furthermore, a comparison study has been conducted with a conventional energy harvesting and storage system consisting of a single leg thermoelectric generator (TEG) based on Bi₂Te₃ connected in series to the same supercapacitor. Besides larger space requirements and circuit complexity, the Seebeck coefficient of Bi₂Te₃ (190 μV K⁻¹) is approximately six times lower than our gel electrolyte which results in 41 times lower energy density (Table S5). Also, we evaluate the efficiency η in converting heat to electricity defined as the ratio between energy stored in the device during thermal charging ($E_{C,ch}$) and waste heat input during that time (Q_{in}), using the equation (S17) derived recently by Wang et al. [4]. The efficiency of our device is quite low ($5 \times 10^{-5}\%$) when compared to the circuit composed of a conventional TEG in series to the same supercapacitor. The low efficiency can be attributed primarily to the low ionic conductivity of the electrolyte used in this study (detailed in Table S4). Future research on improving the ionic conductivity of such electrolytes exhibiting thermoelectric effect is anticipated to result in a higher efficiency.

3. Conclusions

We have demonstrated for the first time that the thermogalvanic effect of the ferrocyanide/ferricyanide redox couple can be used to construct a solid-state thermoelectric supercapacitor. The device stays charged even after the thermal gradient is removed and thus can be discharged by delivering power to an external circuit. Our TCSC consists of two carbon cloth electrodes sandwiching a potassium ferrocyanide/ferricyanide gel electrolyte film. In addition to thermogalvanic effect, the potassium ferrocyanide/ferricyanide redox couple also leads to high capacitance due to its pseudocapacitive property. The fabricated symmetric TCSC device

exhibits excellent electrochemical performance in terms of enhanced capacitance, self-discharge behavior and cyclic stability. Hence, such thermal charging concept offers a simple, low-cost method of storing large amount of energy in a given footprint area from intermittent heat sources without involving any complex electrode fabrication process. An equivalent circuit model representing the device is developed which shows agreement with the current and voltage profiles measured during thermal charging. Based on a fitting technique, the area-specific capacitance value of the TCSC device is determined to be 13.3 F cm⁻² which is more than two orders of magnitude larger than TCSC devices demonstrated in the past.

4. Experimental section

PVA/K₃Fe(CN)₆/K₄Fe(CN)₆ gel fabrication: 4g of polyvinyl alcohol (PVA) powder (molecular weight 89,000–98,000, 99% hydrolyzed Sigma-Aldrich) was dissolved in 40 ml deionized water along with 10 ml solution containing a mixture of 0.1 mol l⁻¹ K₃Fe(CN)₆ and K₄Fe(CN)₆. The solution was heated to 85 °C under continuous stirring, until the solution became clear. The viscous solution was then poured onto a 60 mm PTFE evaporating dish and allowed to evaporate slowly in hood at room temperature for around 24 h. Upon complete evaporation of excess water, a flexible, thin, free standing and semi-transparent polymer gel electrolyte membrane was obtained. It was then cut to the desired shape for supercapacitor assembly. By altering the volume of the viscous gel electrolyte allowed to dry in the PTFE evaporating dish, the membrane thickness could be controlled.

Two-electrode device assembly: Two CC electrodes were immersed into the 85 °C PVA/K₃Fe(CN)₆/K₄Fe(CN)₆ gel electrolyte (the copper contacts kept out) for 10 min and then taken out. The hot electrolyte soaked and penetrated the porous electrodes thoroughly. To assemble the TCSC device, the wet electrodes were clamped together with a polymer gel electrolyte membrane of appropriate thickness, sandwiched in between. The assembly was dried at room temperature for 12 h to vaporize the excess water. Thereafter, the device was packaged in a nylon film bag.

Material characterization: The surface morphology of electrodes was characterized by field emission scanning electron microscope (SEM, Hitachi S-4800).

Electrochemical measurements: Electrochemical measurements were conducted using a Gamry Echem Testing System, Gamry Instruments, Inc., USA. Electrochemical performance of carbon cloth samples were obtained in a three-electrode configuration cell at room temperature using either 1.0 mol l⁻¹ H₃PO₄ or a mixture of 0.2 mol l⁻¹ K₃Fe(CN)₆ and 0.2 mol l⁻¹ K₄Fe(CN)₆ as the electrolyte. Bare CC or CC/GP electrode was used as the working electrode with Pt mesh and standard Ag/AgCl electrode as the counter and reference electrodes respectively.

Thermistor calibration: The thermistor used in the experiments is a micro-betachip thermistor probe procured from Mouser electronics. It was calibrated with a standard Parr 6775 digital thermometer. A comparison of the temperature readings shown in Table S2 shows a maximum error of 0.1%.

Conflicts of interest

TSF hereby informs the journal of his position as Founder and President of TMG Technologies, LLC, a company whose business activities include the development of manufacturing equipment and technical consulting. The submitted work is an unrelated academic study and is not intended or represented as a commercial product or promotion. AK has no conflicts of interest.

Acknowledgements

The authors thank the U.S. Air Force Office of Scientific Research under the MURI program on Nanofabrication of Tunable 3D Nanotube Architectures (PM: Dr. Joycelyn Harrison, Grant: FA9550-12-1-0037) for support of this work. Furthermore, we thank Prof. Ali Shakouri for useful suggestions, Pingge He for assistance on device fabrication, Yuan Hu for assistance on data acquisition and Majed Alrefae for capturing SEM images.

Appendix A. Supplementary data

Supplementary data related to this article can be found at <https://doi.org/10.1016/j.electacta.2018.05.164>.

References

- [1] K. Maize, A. Kundu, G. Xiong, K. Saviers, T.S. Fisher, A. Shakouri, Electroreflectance imaging of gold-h3po4 supercapacitors. part i: experimental methodology, *Analyst* 141 (2016) 1448–1461.
- [2] K.R. Saviers, A. Kundu, K. Maize, A. Shakouri, T.S. Fisher, Electroreflectance imaging of gold-h3po4 supercapacitors. part ii: microsupercapacitor ageing characterization, *Analyst* 141 (2016) 1462–1471.
- [3] D. Zhao, H. Wang, Z.U. Khan, J.C. Chen, R. Gabrielsson, M.P. Jonsson, M. Berggren, X. Crispin, Ionic thermoelectric supercapacitors, *Energy Environ. Sci.* 9 (2016) 1450–1457.
- [4] H. Wang, D. Zhao, Z.U. Khan, S. Puzinas, M.P. Jonsson, M. Berggren, X. Crispin, Ionic thermoelectric figure of merit for charging of supercapacitors, *Adv. Electron. Mater.* 3 (4) (2017), 1700013.
- [5] D. Zhao, S. Fabiano, M. Berggren, X. Crispin, Ionic thermoelectric gating organic transistors, *Nat. Commun.* 8 (2017) 12414.
- [6] M. Bonetti, S. Nakamae, M. Roger, P. Guenoun, Huge seebeck coefficients in nonaqueous electrolytes, *J. Chem. Phys.* 134 (2011), 114513.
- [7] W.B. Chang, H. Fang, J. Liu, C.M. Evans, B. Russ, B.C. Popere, S.N. Patel, M.L. Chabiny, R.A. Segalman, Electrochemical effects in thermoelectric polymers, *ACS Macro Lett.* 5 (4) (2016) 455–459.
- [8] H. Wang, U. Ail, R. Gabrielsson, M. Berggren, X. Crispin, Ionic seebeck effect in conducting polymers, *Adv. Energy Mater.* 5 (11) (2015), 1500044.
- [9] A.H. Kazim, B.A. Cola, Electrochemical characterization of carbon nanotube and poly (3,4-ethylenedioxythiophene)-poly(styrenesulfonate) composite aqueous electrolyte for thermo-electrochemical cells, *J. Electrochem. Soc.* 163 (2016) F867–F871.
- [10] H. Im, H.G. Moon, J.S. Lee, I.Y. Chung, T.J. Kang, Y.H. Kim, Flexible thermocells for utilization of body heat, *Nano Res.* 7 (4) (2014) 443–452.
- [11] A. Kundu, M.A. Alrefae, T.S. Fisher, Magnetothermoelectric effects in graphene and their dependence on scatterer concentration, magnetic field, and band gap, *J. Appl. Phys.* 121 (2017), 125113.
- [12] T. Ikeshoji, Thermoelectric conversion by thin-layer thermogalvanic cells with soluble redox couples, *Bull. Chem. Soc. Jpn.* 60 (1987) 1505.
- [13] T. Quickenden, C. Vernon, Thermogalvanic conversion of heat to electricity, *Sol. Energy* 36 (1986) 63–72.
- [14] B. Burrows, Discharge behavior of redox thermogalvanic cells, *J. Electrochem. Soc.* 123 (1976) 154–159.
- [15] B. Poudel, Q. Hao, Y. Ma, Y. Lan, A. Minnich, B. Yu, X. Yan, D. Wang, A. Muto, D. Vashaee, X. Chen, J. Liu, M.S. Dresselhaus, G. Chen, Z. Ren, High-thermoelectric performance of nanostructured bismuth antimony telluride bulk alloys, *Science* 320 (5876) (2008) 634–638.
- [16] T.J. Abraham, D.R. MacFarlane, J.M. Pringle, High seebeck coefficient redox ionic liquid electrolytes for thermal energy harvesting, *Energy Environ. Sci.* 6 (2013) 2639–2645.
- [17] H. Zhou, T. Yamada, N. Kimizuka, Supramolecular thermo-electrochemical cells: enhanced thermoelectric performance by host-guest complexation and salt-induced crystallization, *J. Am. Chem. Soc.* 138 (33) (2016) 10502–10507.
- [18] R. Hu, B.A. Cola, N. Haram, J.N. Barisci, S. Lee, S. Stoughton, G. Wallace, C. Too, M. Thomas, A. Gestos, M. E. d. Cruz, J.P. Ferraris, A.A. Zakhidov, R.H. Baughman, Harvesting waste thermal energy using a carbon-nanotube-based thermo-electrochemical cell, *Nano Lett.* 10 (3) (2010) 838–846.
- [19] M.S. Romano, N. Li, D. Antiohos, J.M. Razal, A. Nattestad, S. Beirne, S. Fang, Y. Chen, R. Jalili, G.G. Wallace, R. Baughman, J. Chen, Carbon nanotube-reduced graphene oxide composites for thermal energy harvesting applications, *Adv. Mater.* 25 (45) (2013) 6602–6606.
- [20] P.F. Salazar, S. Kumar, B.A. Cola, Nitrogen- and boron-doped carbon nanotube electrodes in a thermo-electrochemical cell, *J. Electrochem. Soc.* 159 (5) (2012) B483–B488.
- [21] P.F. Salazar, S.T. Stephens, A.H. Kazim, J.M. Pringle, B.A. Cola, Enhanced thermo-electrochemical power using carbon nanotube additives in ionic liquid redox electrolytes, *J. Mater. Chem. A* 2 (2014) 20676–20682.
- [22] P. Yang, K. Liu, Q. Chen, X. Mo, Y. Zhou, S. Li, G. Feng, J. Zhou, Wearable thermocells based on gel electrolytes for the utilization of body heat, *Angew. Chem. Int. Ed.* 55 (39) (2016) 12050–12053.
- [23] S.L. Kim, H.T. Lin, C. Yu, Thermally chargeable solid-state supercapacitor, *Adv. Energy Mater.* 6 (18) (2016), 1600546.
- [24] F. Jiao, A. Naderi, D. Zhao, J. Schlueter, M. Shahi, J. Sundstrom, H. Granberg, J. Edberg, U. Ail, J. W. Brill, T. Lindstrom, M. Berggren, X. Crispin, Ionic thermoelectric paper, *J. Mater. Chem. A*.
- [25] L.T. Le, M.H. Ervin, H. Qiu, B.E. Fuchs, W.Y. Lee, Graphene supercapacitor electrodes fabricated by inkjet printing and thermal reduction of graphene oxide, *Electrochem. Commun.* 13 (4) (2011) 355–358.
- [26] A. Yuan, Q. Zhang, A novel hybrid manganese dioxide/activated carbon supercapacitor using lithium hydroxide electrolyte, *Electrochem. Commun.* 8 (7) (2006) 1173–1178.
- [27] C. Meng, C. Liu, S. Fan, Flexible carbon nanotube/polyaniline paper-like films and their enhanced electrochemical properties, *Electrochem. Commun.* 11 (1) (2009) 186–189.
- [28] Y.-C. Chen, Y.-K. Hsu, Y.-G. Lin, Y.-K. Lin, Y.-Y. Horng, L.-C. Chen, K.-H. Chen, Highly flexible supercapacitors with manganese oxide nanosheet/carbon cloth electrode, *Electrochim. Acta* 56 (20) (2011) 7124–7130.
- [29] G. Xiong, K. Hembram, R. Reifemberger, T.S. Fisher, MnO₂-coated graphitic petals for supercapacitor electrodes, *J. Power Sources* 227 (2013) 254–259.
- [30] J. Zhong, L.-Q. Fan, X. Wu, J.-H. Wu, G.-J. Liu, J.-M. Lin, M.-L. Huang, Y.-L. Wei, Improved energy density of quasi-solid-state supercapacitors using sandwich-type redox-active gel polymer electrolytes, *Electrochim. Acta* 166 (2015) 150–156.
- [31] S. Roldan, C. Blanco, M. Granda, R. Menendez, R. Santamaria, Towards a further generation of high-energy carbon-based capacitors by using redox-active electrolytes, *Angew. Chem. Int. Ed.* 50 (7) (2011) 1699–1701.
- [32] S. Senthilkumar, R. Selvan, N. Ponpandian, J. Melo, Redox additive aqueous polymer gel electrolyte for an electric double layer capacitor, *RSC Adv.* 2 (2012) 8937–8940.
- [33] H. Yu, J. Wu, J. Lin, L. Fan, M. Huang, Y. Lin, Y. Li, F. Yu, Z. Qiu, A reversible redox strategy for swcnt-based supercapacitors using a high-performance electrolyte, *ChemPhysChem* 14 (2013) 394–399.
- [34] G. Ma, E. Feng, K. Sun, H. Peng, J. Li, Z. Lei, A novel and high-effective redox-mediated gel polymer electrolyte for supercapacitor, *Electrochim. Acta* 135 (2014) 461–466.
- [35] L.-H. Su, X.-G. Zhang, C.-H. Mi, B. Gao, Y. Liu, Improvement of the capacitive performances for co-al layered double hydroxide by adding hexacyanoferrate into the electrolyte, *Phys. Chem. Chem. Phys.* 11 (2009) 2195–2202.
- [36] J. Lee, S. Choudhury, D. Weingarth, D. Kim, V. Presser, High performance hybrid energy storage with potassium ferricyanide redox electrolyte, *ACS Appl. Mater. Interfaces* 8 (36) (2016) 23676–23687.
- [37] G. Ma, J. Li, K. Sun, H. Peng, J. Mu, Z. Lei, High performance solid-state supercapacitor with pva-koh-k3[fe(cn)6] gel polymer as electrolyte and separator, *J. Power Sources* 256 (2014) 281–287.
- [38] G. Xiong, C. Meng, R.G. Reifemberger, P.P. Irazoqui, T.S. Fisher, Graphitic petal electrodes for all-solid-state flexible supercapacitors, *Adv. Energy Mater.* 4 (3) (2014), 1300515–n/a.
- [39] Y. Tian, J. Yan, R. Xue, B. Yi, Capacitive properties of activated carbon in k4fe(cn)6, *J. Electrochem. Soc.* 158 (7) (2011) A818–A821.
- [40] K. Chen, F. Liu, D. Xue, S. Komarneni, Carbon with ultrahigh capacitance when graphene paper meets k3fe(cn)6, *Nanoscale* 7 (2015) 432–439.
- [41] A.J. Bard, L.R. Faulkner, *Electrochemical Methods: Fundamentals and Applications*, 2001.
- [42] C. Punckt, M.A. Pope, I.A. Aksay, On the electrochemical response of porous functionalized graphene electrodes, *J. Phys. Chem. C* 117 (31) (2013) 16076–16086.
- [43] S.T. Senthilkumar, R.K. Selvan, Flexible fiber supercapacitor using biowaste-derived porous carbon, *ChemElectroChem* 2 (8) (2015) 1111–1116.
- [44] Y. Gogotsi, P. Simon, True performance metrics in electrochemical energy storage, *Science* 334 (6058) (2011) 917–918.
- [45] M.D. Stoller, R.S. Ruoff, Best practice methods for determining an electrode material's performance for ultracapacitors, *Energy Environ. Sci.* 3 (2010) 1294–1301.
- [46] J.R. Miller, Valuing reversible energy storage, *Science* 335 (6074) (2012) 1312–1313.
- [47] R.B. Rakhi, B. Ahmed, M.N. Hedhili, D.H. Anjum, H.N. Alshareef, Effect of postetch annealing gas composition on the structural and electrochemical properties of ti2ctx mxene electrodes for supercapacitor applications, *Chem. Mater.* 27 (15) (2015) 5314–5323.
- [48] J. Xu, S. Gai, F. He, N. Niu, P. Gao, Y. Chen, P. Yang, A sandwich-type three-dimensional layered double hydroxide nanosheet array/graphene composite: fabrication and high supercapacitor performance, *J. Mater. Chem. A* 2

- (2014) 1022–1031.
- [49] J. Zhong, L.-Q. Fan, X. Wu, J.-H. Wu, G.-J. Liu, J.-M. Lin, M.-L. Huang, Y.-L. Wei, Improved energy density of quasi-solid-state supercapacitors using sandwich-type redox-active gel polymer electrolytes, *Electrochim. Acta* 166 (2015) 150–156.
- [50] L. Chen, H. Bai, Z. Huang, L. Li, Mechanism investigation and suppression of self-discharge in active electrolyte enhanced supercapacitors, *Energy Environ. Sci.* 7 (2014) 1750–1759.
- [51] D.-Z. Chen, J. Yu, W. Lu, Y. Zhao, Y. Yan, T.-W. Chou, Temperature effects on electrochemical performance of carbon nanotube film based flexible all-solid-state supercapacitors, *Electrochim. Acta* 233 (2017) 181–189.